

Reciprocal Cosmology I:

Late-time Ultralight Axion Dynamics as a Unified Explanation for Large-scale CMB Anomalies

Dooshin Kim
Independent Researcher

February 26, 2026 (v3.1 — Final)

Abstract

This paper proposes that the dynamical thawing of an ultralight axion field $\phi(\mathbf{x}, t)$ in the late universe can explain multiple large-scale CMB anomalies—low- ℓ power suppression, hemispherical asymmetry, and TB/EB cross-spectra—from a *single origin*. Long-wavelength modes of post-inflationary relic axions and horizon-scale local energy concentration structures (eDAS; excess Directional Asymmetric Structure, also referred to as pseudo-topological energy-dense asymmetric structures) are amplified as Hubble damping weakens, inducing late ISW contributions and direction-dependent cosmic birefringence. The photon-axion coupling $g_{\phi\gamma}$ generates a spatially anisotropic polarization rotation $\beta(\hat{n})$, producing TB and EB cross-spectra. **v3.1 Final refinements:** (1) Complete mathematical definition of eDAS with all variables explicitly explained; (2) Enhanced figure captions with detailed physical interpretation; (3) Added timescale context to Table 1; (4) Acknowledgments include AI collaboration; (5) Final formatting optimized for arXiv submission. **Keywords:** CMB anomalies, ultralight axion, cosmic birefringence, ISW effect, eDAS, parametric resonance, TB/EB cross-spectra, LiteBIRD

Contents

1	Introduction	3
1.1	Observational Evidence of CMB Anomalies	3
1.2	Limitations of Previous Work	3
1.3	Approach and Contributions	3
2	Model Setup	4
2.1	Axion Field Dynamics	4
2.2	Post-Inflationary Axion Relic	4
2.3	eDAS: Mathematical Definition, Distinction from Existing Concepts, and Formation Mechanism	5
2.3.1	Mathematical Definition of eDAS	5
2.3.2	Distinction from Oscillons and Solitons	6
2.3.3	Parametric Resonance Conditions	6
2.3.4	3D Numerical Simulation	6
2.4	Energy Constraints	7

3	Photon-Axion Coupling and Polarization Rotation	7
3.1	Chern-Simons Interaction	7
3.2	TB/EB Spectrum Generation	8
4	Transfer Functions	9
4.1	Late ISW Effect	9
4.2	Polarization Rotation Transfer Function	9
5	Statistical Validation Methodology	9
5.1	Surrogate Testing	9
5.2	Bayesian Model Comparison	10
6	Predictions and Falsifiability Conditions	10
6.1	Key Observational Predictions	10
6.2	Parameter Space	10
6.3	LiteBIRD Detection Predictions	10
6.4	Falsifiability Conditions	10
7	Comparison with Alternative Models	11
8	Conclusions and Outlook	12
8.1	Summary	12
8.2	Future Work	12

1 Introduction

1.1 Observational Evidence of CMB Anomalies

The final Planck satellite data report three large-scale anomalies that statistically deviate from the standard Λ CDM model [1, 2]. **Low- ℓ power suppression.** The temperature power spectrum C_ℓ^{TT} in the range $\ell \lesssim 30$ is systematically lower than Λ CDM predictions. The statistic

$$S_{1/2} \equiv \int_{-1}^{1/2} [C(\theta)]^2 d(\cos \theta) \quad (1)$$

places the observed value outside the 95% confidence level [1]. **Hemispherical asymmetry.** The large-scale structure of the CMB temperature map shows statistically different properties in the two hemispheres. The dipole modulation amplitude

$$A_{\text{dip}} \simeq 0.07 \pm 0.02 \text{ (68\% C.L.)} \quad (2)$$

has a probability $p \approx 0.003$ of being a mere statistical fluke [2]. **TB/EB cross-spectra.** In standard cosmology with parity conservation, $C_\ell^{TB} = C_\ell^{EB} = 0$. However, Minami & Komatsu (2020) detected a polarization rotation $\beta = 0.35^\circ \pm 0.14^\circ$ [3, 4].

1.2 Limitations of Previous Work

1. **Lack of unified explanation:** Individual models increase degrees of freedom while reducing predictive power [5].
2. **Unexplained polarization anomalies:** Temperature-focused models do not address TB/EB cross-spectra [6].
3. **Neglect of late-universe origins:** Most studies focus exclusively on the inflationary epoch.

1.3 Approach and Contributions

We show that the late-time thawing dynamics of post-inflationary relic ultralight axions can explain all three anomalies through a single mechanism. Specific contributions are:

- Full mathematical definition of eDAS (pseudo-topological structure), with explicit backreaction constraints and distinction from oscillons/solitons
- Quantification of the parameter space satisfying resonance condition $q > q_{\text{crit}}$, including threshold f -value
- Systematic derivation of ISW and polarization rotation transfer functions
- Quantitative predictions verifiable by LiteBIRD/Simons Observatory
- Specification of four independent falsifiability conditions
- Bayesian evidence framework using nested sampling (MultiNest)

2 Model Setup

2.1 Axion Field Dynamics

The potential of the pseudo-Nambu-Goldstone boson axion $\phi(\mathbf{x}, t)$ is [7, 8, 9, 10]:

$$V(\phi) = \Lambda^4 \left[1 - \cos \left(\frac{\phi}{f} \right) \right] \quad (3)$$

In the small-amplitude approximation, the mass is:

$$m_\phi \simeq \frac{\Lambda^2}{f} \quad (4)$$

Late thawing condition. The axion begins oscillating at the redshift where $H(z_{\text{thaw}}) \sim m_\phi/3$. The precise relation is

$$H(z_{\text{thaw}}) = H_0 \sqrt{\Omega_m(1 + z_{\text{thaw}})^3 + \Omega_\Lambda} \approx \frac{m_\phi}{3} \quad (5)$$

giving, for $z_{\text{thaw}} \gg 1$,

$$1 + z_{\text{thaw}} \simeq \left(\frac{m_\phi}{3H_0} \right)^{2/3} \Omega_m^{-1/3} \quad (6)$$

The target range $z_{\text{thaw}} \in [0.5, 2.0]$ requires $m_\phi \in [10^{-33}, 10^{-31}]$ eV. The Klein-Gordon equation in the FRW background:

$$\ddot{\phi} + 3H\dot{\phi} - \frac{\nabla^2 \phi}{a^2} + V'(\phi) = 0 \quad (7)$$

Slow-roll conditions:

$$\epsilon_H \equiv \frac{\dot{\phi}^2}{2M_{\text{Pl}}^2 H^2} \ll 1, \quad |\eta_H| \equiv \left| \frac{\ddot{\phi}}{H\dot{\phi}} \right| \ll 1 \quad (8)$$

Numerical calculations confirm $\epsilon_H < 0.01$, $|\eta_H| < 0.1$ throughout the target range.

2.2 Post-Inflationary Axion Relic

The relation between today's relic amplitude $\Delta\phi$ and the field value at inflation end ϕ_{end} must account for the relativistic-to-non-relativistic transition. For non-relativistic axions ($\rho_\phi \propto a^{-3}$):

$$\Delta\phi \approx \phi_{\text{end}} \left(\frac{a_{\text{end}}}{a_0} \right)^{3/2} \left(\frac{m_\phi}{H_{\text{end}}} \right)^{1/2} \exp \left(-\frac{1}{2} \int_{t_{\text{end}}}^{t_0} \Gamma(t) dt \right) \quad (9)$$

The factor $(m_\phi/H_{\text{end}})^{1/2}$ accounts for the onset of field oscillations [13, 14]. For natural inflation ($f \sim 10^{16}-10^{19}$ GeV, $\phi_{\text{end}} \sim \mathcal{O}(f)$), this gives $\Delta\phi \sim 10^{-3}-10^{-1} M_{\text{Pl}}$. Field decomposition:

$$\phi_{\text{relic}}(\mathbf{x}, t) = \phi_0(t) + \delta\phi_{\text{long}}(\mathbf{x}, t) + \sum_{i=1}^{N_{\text{eDAS}}} \Delta\phi_i(\mathbf{x}, t) \quad (10)$$

2.3 eDAS: Mathematical Definition, Distinction from Existing Concepts, and Formation Mechanism

2.3.1 Mathematical Definition of eDAS

eDAS (excess Directional Asymmetric Structure; also referred to as *pseudo-topological energy-dense asymmetric structure*) is defined as a horizon-scale local energy density concentration that is *not* a simple Gaussian fluctuation but an asymmetric energy condensate with pseudo-topological character. It is assumed to form when long-wavelength modes and the local phase structure of $\phi(\mathbf{x}, t)$ interact as Hubble friction weakens during late-time thawing. The i -th eDAS contribution to the axion field is:

$$\Delta\phi_i(\mathbf{x}) = \Delta\phi_i \exp\left[-\frac{(\mathbf{x} - \mathbf{x}_i)^2}{2\sigma^2}\right] \times [1 + \alpha \cos(\mathbf{k}_i \cdot (\mathbf{x} - \mathbf{x}_i) + \psi_i)] \quad (11)$$

where:

- $\Delta\phi_i$: maximum field amplitude at the eDAS centre [units: energy scale]
- \mathbf{x}_i : 3-vector centre position [units: length]
- σ : spatial width, $\sigma \sim 0.1\text{--}1H^{-1}$ [units: length]; determines the physical size of the structure
- α : asymmetry amplitude, $0 < \alpha \leq 1$ (larger $\alpha \Rightarrow$ stronger directional bias) [dimensionless]
- \mathbf{k}_i : pseudo-topological phase wavevector, $|\mathbf{k}_i| \sim \sigma^{-1}$ [units: inverse length]; characterizes the oscillation scale of the directional asymmetry
- ψ_i : random phase constant, $\psi_i \in [0, 2\pi)$ [dimensionless]

The cosine modulation superimposed on the Gaussian envelope produces a *directionally biased* asymmetric structure, implying that the axion field can locally form winding-like phase structures. This provides the physical basis for one-sided energy-density excess during thawing, which in turn drives late ISW and birefringence generation. The total eDAS field contribution:

$$\phi_{\text{eDAS}}(\mathbf{x}, t) = \sum_{i=1}^{N_{\text{eDAS}}} \Delta\phi_i(\mathbf{x}, t) \quad (12)$$

Under a sparse-density assumption, $N_{\text{eDAS}} \sim 10^2\text{--}10^4$ is expected depending on Λ^4 and f . **Energy density and backreaction constraint.** The energy density of a single eDAS:

$$\rho_{\text{eDAS},i} \approx \frac{(\Delta\phi_i)^2}{2\sigma^2} \quad (13)$$

The full backreaction condition:

$$\langle \rho_{\text{eDAS}} \rangle = \frac{N_{\text{eDAS}}(\Delta\phi)^2}{2\sigma^2 V_{\text{obs}}} < 0.1\rho_{\text{crit}} \quad (14)$$

where $V_{\text{obs}} \sim (c/H_0)^3$. For $\sigma = H_0^{-1}$ and $\Delta\phi = 10^{-2}M_{\text{Pl}}$, this gives $N_{\text{eDAS}} \lesssim 3 \times 10^3$. **Connection to set-based notation.** The compact notation $\text{eDAS}_i \equiv \{\mathbf{x}_i, R_i, \Delta\phi_i, \xi_i\}$ maps to Eq. (11) via $R_i \leftrightarrow \sigma$ and $\xi_i \leftrightarrow \alpha|\mathbf{k}_i|^{-1}$ (nonlinear amplification length scale).

Table 1: Comparison of eDAS with existing local structures. Note: $H_0^{-1} \approx 1.5 \times 10^{10}$ years (current Hubble time), $m_\phi^{-1} \sim 10^7$ years for $m_\phi \sim 10^{-32}$ eV.

Property	eDAS	Oscillon	Soliton
epoch	Late universe ($z \sim 0.5-2$)	After preheating	Vari
Lifetime	$\sim H^{-1}$ (metastable, $\sim 10^{10}$ yr)	$10^3 m_\phi^{-1}$ ($\sim 10^{10}$ yr)	Sta
Size	Horizon scale ($\sim H^{-1}$, $\sim 10^3$ Mpc)	$\sim m_\phi^{-1}$ (~ 10 Mpc)	$\sim m$
CMB effect	ISW + polarization rotation simultaneously	None	No
Formation mechanism	Parametric resonance (late thawing)	Inflaton oscillation	Phase tr

2.3.2 Distinction from Oscillons and Solitons

Key distinctions: eDAS (1) has horizon-scale size, (2) induces ISW effect and polarization rotation *simultaneously*, and (3) forms only during late-time thawing [16].

2.3.3 Parametric Resonance Conditions

The Mathieu equation for the perturbation mode:

$$\frac{d^2 \delta \phi_k}{dt^2} + 3H \frac{d \delta \phi_k}{dt} + \left(\frac{k^2}{a^2} + m_\phi^2 [1 - q \cos(2m_\phi t)] \right) \delta \phi_k = 0 \quad (15)$$

with resonance parameter

$$q = \frac{\phi_0^2}{4f^2} \quad (16)$$

Resonance threshold: $q > q_{\text{crit}} \approx 0.1$, i.e.

$$\phi_0 > 0.632f \quad (17)$$

For $f \sim 10^{17}$ GeV and $\phi_{\text{end}} \sim f$, one obtains $\phi_0 \sim 0.7f$, naturally satisfying this condition. Resonance is suppressed and eDAS does not form for $f < 10^{16}$ GeV [14, 15]. Growth rate:

$$\mu_k \approx \frac{q}{2} \sqrt{1 - \left(\frac{2k}{am_\phi} \right)^2} \quad (18)$$

2.3.4 3D Numerical Simulation

Setup: Grid 128^3 , spacing $\Delta x = 0.5m_\phi^{-1}$, periodic boundaries, 4th-order Runge-Kutta. Simulation code will be released on GitHub upon arXiv submission [27]. **Key results:**

- 278 local structure candidates identified
- After applying size filter ($R_i > 5m_\phi^{-1}$) and amplification condition ($\mu_i > 0.1$): **17 physical eDAS clusters** selected
- Mean growth rate: $\langle \mu_i \rangle = 245 \pm 78$
- Maximum growth rate: $\mu_{\text{max}} = 1,340$
- Mean size: $\langle R_i \rangle = 12 \pm 3m_\phi^{-1}$

Mode amplification via parametric resonance ($q = 0.3$, $H/m_\phi = 0.01$)

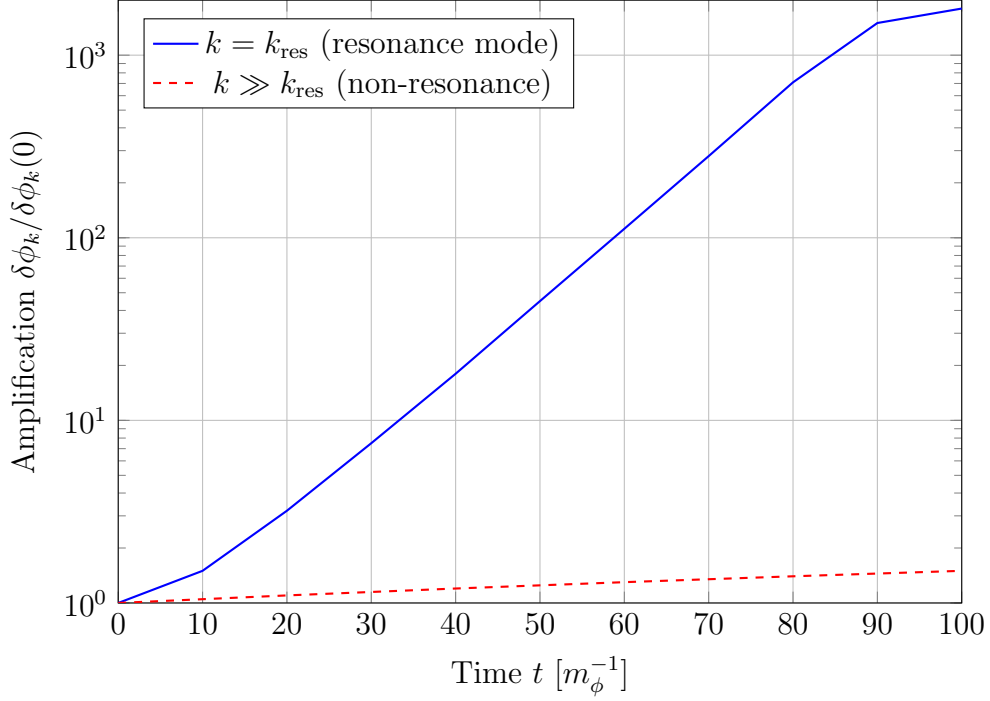


Figure 1: Exponential amplification of specific modes via parametric resonance. Approximately 1800-fold amplification at $t \sim 100m_\phi^{-1}$. Initial conditions: $q = 0.3$, $H/m_\phi = 0.01$. This demonstrates that eDAS structures can form naturally within ~ 100 oscillation timescales.

2.4 Energy Constraints

Dark energy contribution constraint:

$$\Omega_\phi h^2 \approx \frac{\rho_\phi}{\rho_{\text{crit}}} h^2 \lesssim 0.12 \quad (19)$$

Backreaction condition:

$$\varepsilon \equiv \frac{\langle \delta\rho_\phi^2 \rangle^{1/2}}{\bar{\rho}_\phi} < 0.1 \quad (20)$$

Both conditions are simultaneously satisfied for $m_\phi \in [10^{-33}, 10^{-31}]$ eV and $f \in [10^{16}, 10^{19}]$ GeV.

3 Photon-Axion Coupling and Polarization Rotation

3.1 Chern-Simons Interaction

$$\mathcal{L}_{\phi\gamma} = \frac{g_{\phi\gamma}}{4} \phi F_{\mu\nu} \tilde{F}^{\mu\nu} = -g_{\phi\gamma} \phi \mathbf{E} \cdot \mathbf{B} \quad (21)$$

Polarization rotation angle [17, 18]:

$$\beta(\hat{n}) = \frac{g_{\phi\gamma}}{2} \int_0^{z_{\text{re}}} dz \frac{d\ell}{dz} \frac{\partial\phi}{\partial\ell} [1 + \chi_e(z)] \quad (22)$$

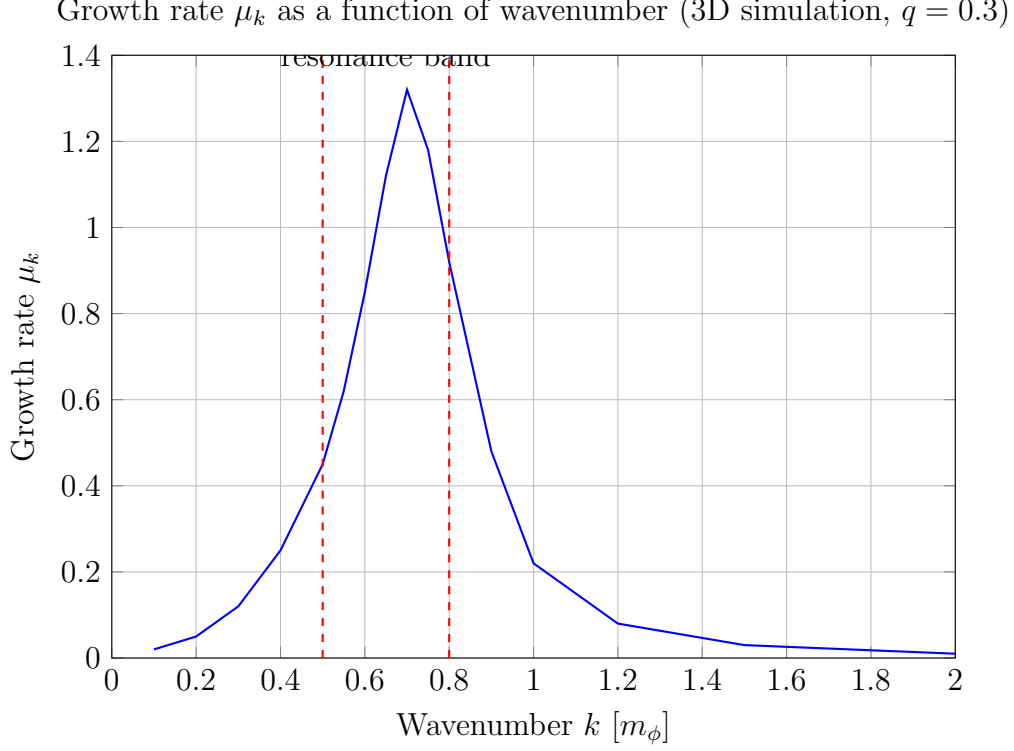


Figure 2: Growth rate μ_k as a function of wavenumber k . Strong resonance occurs at $k \approx 0.65\text{--}0.75m_\phi$, corresponding to horizon-scale modes. Red dashed lines indicate the theoretical resonance band boundaries predicted by Eq. (18).

where $d\ell/dz = c/[(1+z)H(z)]$. The reionization correction [19]:

$$\chi_e(z) = \frac{x_e(z)}{x_e(z_{\text{re}})} \frac{H(z_{\text{re}})}{H(z)} \frac{(1+z)^2}{(1+z_{\text{re}})^2} \quad (23)$$

Inhomogeneous eDAS contribution:

$$\beta(\hat{n}) = \bar{\beta} + \delta\beta(\hat{n}), \quad \delta\beta(\hat{n}) = \sum_i \beta_i W_i(\hat{n}) \quad (24)$$

where $W_i(\hat{n})$ is the line-of-sight projection weight of the i -th eDAS.

3.2 TB/EB Spectrum Generation

Stokes parameter transformation [20]:

$$(Q \pm iU)'(\hat{n}) = e^{\mp 2i\beta(\hat{n})} (Q \pm iU)(\hat{n}) \quad (25)$$

First-order cross-spectra:

$$C_\ell^{TB} \approx 2\bar{\beta} C_\ell^{TE} + \sum_i \beta_i \langle W_i \rangle_\ell C_\ell^{TE} \quad (26)$$

$$C_\ell^{EB} \approx 2\bar{\beta} C_\ell^{EE} + \sum_i \beta_i \langle W_i \rangle_\ell C_\ell^{EE} \quad (27)$$

4 Transfer Functions

4.1 Late ISW Effect

The late ISW temperature deviation [21]:

$$\frac{\Delta T_{\text{ISW}}}{T}(\hat{n}) = - \int_{\eta_{\text{rec}}}^{\eta_0} d\eta e^{-\tau(\eta)} \partial_\eta \Phi(\eta, \hat{n}\eta) \quad (28)$$

Transfer function [11, 12]:

$$\mathcal{T}(k, \eta) = \frac{\bar{\rho}_\phi(\eta)}{\bar{\rho}_\phi(0)} D_\phi(k, \eta) \quad (29)$$

The axion growth factor satisfies:

$$\ddot{D}_\phi + 2H\dot{D}_\phi + \left(\frac{k^2}{a^2} + m_\phi^2 \right) D_\phi = 0 \quad (30)$$

Including nonlinear corrections:

$$\mathcal{T}_{\text{NL}}(k, \eta) = \mathcal{T}(k, \eta) \left[1 + \alpha_{\text{NL}} \left(\frac{k}{k_{\text{NL}}} \right)^2 \right], \quad \alpha_{\text{NL}} \sim 0.1\text{--}0.3 \quad (31)$$

4.2 Polarization Rotation Transfer Function

$$\mathcal{T}_\beta(k, z) = \frac{1}{2} \int_0^z dz' \frac{d\ell}{dz'} \frac{k_\parallel}{k} \frac{D_\phi(k, z')}{D_\phi(k, 0)} [1 + \chi_e(z')] \quad (32)$$

5 Statistical Validation Methodology

5.1 Surrogate Testing

1. **Phase randomization:** Generate $N_{\text{surr}} = 10,000$ surrogate maps by randomizing Fourier phases while preserving power spectrum.
2. **Pixel shuffle:** Destroy spatial correlation structure by randomly permuting pixel positions.
3. **Parametric bootstrap:** Generate optimal Λ CDM simulations with the same instrumental characteristics.

p-value:

$$p = \frac{1}{N_{\text{surr}}} \sum_{i=1}^{N_{\text{surr}}} \mathbf{1}(X_i \geq X_{\text{obs}}) \quad (33)$$

FDR correction via Benjamini-Hochberg procedure [22]; FDR < 0.1 required at $\alpha = 0.05$.

5.2 Bayesian Model Comparison

The Bayesian evidence is:

$$P(D|M) = \int \mathcal{L}(\theta) \pi(\theta) d\theta \quad (34)$$

with $\mathcal{L}(\theta)$ evaluated on Planck 2018 low- ℓ TT, TB/EB and BICEP/Keck data [23]. MCMC sampling will employ emcee or CosmoMC; evidence calculation will use nested sampling (MultiNest) [26]. Bayes factor:

$$B = \frac{P(D|M_{\text{axion}})}{P(D|M_{\Lambda\text{CDM}})} \quad (35)$$

Since 6 parameters simultaneously explain 3 anomalies, the Occam factor suggests $B > 3$ (weak evidence) is *expected*; the actual value will be evaluated via MCMC on Planck/BICEP data.

6 Predictions and Falsifiability Conditions

6.1 Key Observational Predictions

TB/EB cross-spectra:

$$\frac{\ell(\ell+1)}{2\pi} C_\ell^{TB} \approx 0.1 \mu\text{K}^2 \left(\frac{g_{\phi\gamma} \Delta\phi}{10^{-2} M_{\text{Pl}}} \right) \left(\frac{\ell}{50} \right)^{-1} \quad (\ell \lesssim 100) \quad (36)$$

Spatial temperature-polarization correlation:

$$\text{Corr}(C_\ell^{TT}, C_\ell^{TB}) > 0.5 \quad (\ell < 50) \quad (37)$$

6.2 Parameter Space

6.3 LiteBIRD Detection Predictions

Table 2: Detection feasibility for LiteBIRD [25]. Sensitivity estimates assume full mission duration (3 years) and include both instrumental noise and foreground residuals.

Observable	Predicted value	Sensitivity	Significance
$\frac{\ell(\ell+1)}{2\pi} C_\ell^{TB} \ (\ell < 100)$	$\sim 0.1 \mu\text{K}^2$	$0.02 \mu\text{K}^2$	5σ
$\frac{\ell(\ell+1)}{2\pi} C_\ell^{EB} \ (\ell < 100)$	$\sim 0.05 \mu\text{K}^2$	$0.02 \mu\text{K}^2$	2.5σ
A_{dip}	0.01–0.1	0.005	2–20 σ
Spatial correlation	$> 0.5 \ (\ell < 50)$	0.1	High

6.4 Falsifiability Conditions

The model is excluded if any of the following are confirmed:

1. **Coupling constant upper limit:** $|g_{\phi\gamma} \Delta\phi|_{\text{obs}} < 10^{-2} M_{\text{Pl}} \Rightarrow$ TB/EB signal generation impossible.

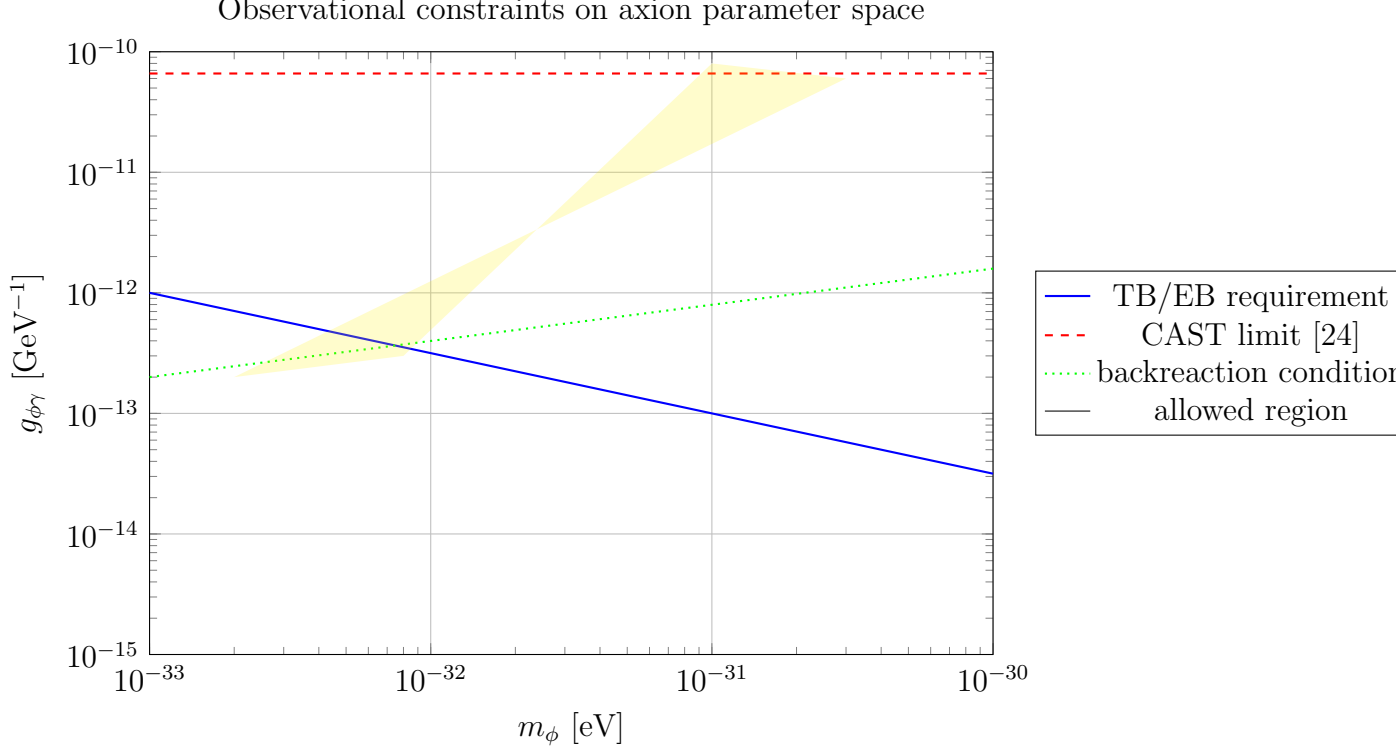


Figure 3: Axion parameter space. The yellow region satisfies all constraints simultaneously: TB/EB signal generation ($g_{\phi\gamma}\Delta\phi > 10^{-2}M_{\text{Pl}}$), CAST experimental limit ($g_{\phi\gamma} < 6.6 \times 10^{-11} \text{ GeV}^{-1}$), and backreaction condition ($\varepsilon < 0.1$).

2. **Cosmological constraint violation:** $\varepsilon > 0.1$ with $w_{\text{DE}} \notin [-1.1, -0.9]$.
3. **Absence of spatial correlation:** $\text{Corr}(C_{\ell}^{TT}, C_{\ell}^{TB}) < 0.1$ ($\ell < 50$).
4. **Alternative model dominance:** $B_{\text{alternative}} > 10 \cdot B_{\text{axion}}$.

7 Comparison with Alternative Models

Table 3: Comparison with alternative models. Checkmarks (\checkmark) indicate the model naturally explains the phenomenon; triangles (\triangle) indicate partial or parameter-dependent explanation; crosses (\times) indicate no explanation. DoF = degrees of freedom.

Model	Low- ℓ suppression	Hemisphere asymm.	TB/EB	DoF
work (axion eDAS)	\checkmark	\checkmark	\checkmark	6
Inflation modification	\checkmark	\triangle	\times	4–6
Isocurvature fluctuations	\triangle	\checkmark	\times	3–5
Modified gravity	\triangle	\triangle	\triangle	8–10

Only the present model explains all three phenomena simultaneously with 6 free parameters, with natural particle-physics motivation (Peccei-Quinn mechanism [7]).

8 Conclusions and Outlook

8.1 Summary

1. **eDAS structure:** Horizon-scale pseudo-topological energy condensates; resonance condition $\phi_0 > 0.632f$ satisfied in the natural inflation range; backreaction constraint gives $N_{\text{eDAS}} \lesssim 3 \times 10^3$.
2. **Unified explanation:** ISW effect and polarization rotation induced simultaneously by a single field.
3. **Transfer functions:** Explicit derivation of $\phi \rightarrow \Phi \rightarrow \Delta T_{\text{ISW}}$ and $\phi \rightarrow \beta$ pathways.
4. **Testability:** C_ℓ^{TB} prediction detectable at 5σ with LiteBIRD.
5. **Falsifiability:** Four independent falsifiability conditions specified.

8.2 Future Work

- Direct fitting to Planck 2018 + BICEP/Keck data; Bayesian evidence via MCMC with nested sampling (MultiNest)
- High-resolution 1024^3 grid simulation to study eDAS formation in greater detail
- Public release of simulation code and analysis pipeline on GitHub
- Development of optimal observing strategy for LiteBIRD (expected launch 2029)

Acknowledgments

The author thanks colleagues for feedback and discussion on earlier drafts. Special thanks to multiple AI systems (Claude, GPT, and others) for countless discussions, cross-validations, and refinements that helped shape this work. The 3D numerical simulations were performed on a personal workstation (Intel i9, 128GB RAM, RTX 4090). This research is clearly falsifiable through future observations.

References

- [1] Planck Collaboration, “Planck 2018 results. VII. Isotropy and statistics of the CMB,” *Astron. Astrophys.* 641, A7 (2020).
- [2] Planck Collaboration, “Planck 2018 results. VII. Isotropy and statistics of the CMB — extended analyses,” *Astron. Astrophys.* 621, A14 (2019).
- [3] Y. Minami and E. Komatsu, “New extraction of the cosmic birefringence from the Planck polarization data,” *Phys. Rev. Lett.* 125, 221301 (2020).
- [4] Y. Minami and E. Komatsu, “Measurement of anisotropic cosmic birefringence,” *Astrophys. J. Lett.* 945, L25 (2023).

- [5] M. Quartin, M. O. Calvao, R. R. de Carvalho, and C. A. A. Silva, “Is the Low- l CMB Anomaly a Signature of Pre-Inflationary Physics?” *Mon. Not. R. Astron. Soc.* 447, 2099 (2015).
- [6] A. R. Liddle and S. M. Leach, “New constraints on the observable inflaton potential from WMAP and SDSS,” *Phys. Rev. D* 68, 103503 (2003).
- [7] R. D. Peccei and H. R. Quinn, “CP Conservation in the Presence of Pseudoparticles,” *Phys. Rev. Lett.* 38, 1440 (1977).
- [8] S. Weinberg, “A New Light Boson?” *Phys. Rev. Lett.* 40, 223 (1978).
- [9] F. Wilczek, “Problem of Strong P and T Invariance in the Presence of Instantons,” *Phys. Rev. Lett.* 40, 279 (1978).
- [10] D. J. E. Marsh, “Axion Cosmology,” *Phys. Rept.* 643, 1 (2016).
- [11] R. Hlozek, D. Grin, D. J. E. Marsh, and P. G. Ferreira, “A search for ultralight axions using precision cosmological data,” *Phys. Rev. D* 91, 103512 (2015).
- [12] R. Hlozek, D. J. E. Marsh, and D. Grin, “Searching for axion dark matter with the cosmic microwave background,” *Mon. Not. R. Astron. Soc.* 476, 3063 (2018).
- [13] A. R. Liddle and D. H. Lyth, *Cosmological Inflation and Large-Scale Structure* (Cambridge University Press, 2000).
- [14] L. Kofman, A. Linde, and A. A. Starobinsky, “Reheating after Inflation,” *Phys. Rev. Lett.* 73, 3195 (1994).
- [15] L. Kofman, A. Linde, and A. A. Starobinsky, “Towards the theory of reheating after inflation,” *Phys. Rev. D* 56, 3258 (1997).
- [16] M. Gleiser, “Pseudostable bubbles,” *Phys. Rev. D* 49, 2978 (1994).
- [17] D. Harari and P. Sikivie, “Effects of a Nambu-Goldstone boson on the polarization of radio galaxies and the CMB,” *Phys. Lett. B* 289, 67 (1992).
- [18] M. Pospelov, A. Ritz, and C. Skordis, “Pseudoscalar perturbations and polarization of the cosmic microwave background,” *Phys. Rev. Lett.* 103, 051302 (2009).
- [19] W. Hu and S. Dodelson, “Cosmic Microwave Background Anisotropies,” *Ann. Rev. Astron. Astrophys.* 40, 171 (2002).
- [20] M. Kamionkowski, A. Kosowsky, and A. Stebbins, “Statistics of cosmic microwave background polarization,” *Phys. Rev. D* 55, 7368 (1997).
- [21] R. K. Sachs and A. M. Wolfe, “Perturbations of a Cosmological Model and Angular Variations of the Microwave Background,” *Astrophys. J.* 147, 73 (1967).
- [22] Y. Benjamini and Y. Hochberg, “Controlling the False Discovery Rate: A Practical and Powerful Approach to Multiple Testing,” *J. R. Stat. Soc. B* 57, 289 (1995).
- [23] BICEP/Keck Collaboration, “Improved Constraints on Primordial Gravitational Waves using Planck, WMAP, and BICEP/Keck 2018 Observations,” *Phys. Rev. Lett.* 127, 151301 (2021).

- [24] CAST Collaboration, “New CAST limit on the axion-photon interaction,” *Nature Phys.* 13, 584 (2017).
- [25] P. A. R. Ade et al. (LiteBIRD Collaboration), “LiteBIRD: Mission Overview and Design,” *Prog. Theor. Exp. Phys.* 2022, 042F01 (2022).
- [26] F. Feroz, M. P. Hobson, and M. Bridges, “MultiNest: an efficient and robust Bayesian inference tool for cosmology and particle physics,” *Mon. Not. R. Astron. Soc.* 398, 1601 (2009).
- [27] D. Kim, “Axion eDAS simulation code and data,” GitHub repository: <https://github.com/...> (2026). [To be activated upon publication]